Environ. Sci. Technol. **2005**, *39,* 2679−2685

Characterization of Adsorption Sites on Aggregate Soil Samples Using Synchrotron X-ray Computerized Microtomography

SUSAN J. ALTMAN,*,† MARK L. RIVERS,‡ MARISSA D. RENO,† RANDALL T. CYGAN,§ AND ANGELA A. MCLAIN†

Geohydrology Department, Sandia National Laboratories, Albuquerque, New Mexico 87185-0735, CARS, University of Chicago, 5640 South Ellis Avenue, Chicago, Illinois 60637, and Geochemistry Department, Sandia National Laboratories, Albuquerque, New Mexico 87185-0750

Synchrotron-source X-ray computerized microtomography (CMT) was used to evaluate the adsorptive properties of aggregate soil samples. A linear relationship between measured mean mass attenuation coefficient (σ) and mass fraction iron was generated by imaging mineral standards with known iron contents. On the basis of reported stoichiometries of the clay minerals and identifications of iron oxyhydroxides (*1*), we calculated the mass fraction iron and iron oxyhydroxide in the intergranular material. The mass fractions of iron were estimated to range from 0.17 to 0.22 for measurements made at 18 keV and from 0.18 to 0.21 for measurements made at 26 keV. One aggregate sample also contained regions within the intergranular material with mass fraction iron ranging from 0.29 to 0.31 and from 0.33 to 0.36 for the 18 and 26 keV measurements, respectively. The mass fraction iron oxyhydroxide ranged from 0.18 to 0.35 for the low-iron intergranular material and from 0.40 to 0.59 for the high-iron intergranular material. Using absorption edge difference imaging with CMT, we visualized cesium on the intergranular material, presumably because of adsorption and possible exchange reactions. By characterizing the mass fraction iron, the mass fraction iron oxyhydroxide, and the adsorptive capacity of these soil mineral aggregates, we provide information useful for conceptualization, development, and parametrization of transport models.

Introduction

Adsorption of dissolved species onto immobile minerals is a recognized mechanism for the retardation of the transport of metals in the subsurface. The extent to which different metal species are retarded must be understood to predict and model the extent of contaminant transport. Examples of such metals include radioisotopes of cesium (Cs^+) and uranium (as uranyl ion, UO_2^{2+}). Cesium has been introduced into the environment because of nuclear weapons testing, nuclear accidents such as Chernobyl, and leakage to groundwater at DOE sites such as Hanford and the Savannah River site. Uranium transport is of interest in the characterization and remediation of waste sites that are contaminated because of mining operations, mill tailings, explosive testings, and natural occurrence. Both cesium and uranium are of critical interest in the study of long-term nuclear waste disposal.

The kinetics and degree of reversibility of the cesium adsorption process are dependent on the mineral substrates to which the metals are adsorbing. Initial adsorption of cesium onto illite is rapid and reversible (*2*) but irreversible on the interlayer sites of bentonite (*3*). Cesium adsorption on humic acid and sand is reversible (*3*). Iron-containing granite fracture-filling materials adsorb cesium in a nonlinear (highly irreversible) fashion (*4*). Some studies indicate that cesium adsorption onto iron oxides is poor relative to clay minerals (*5*, *6*). Other studies indicate that iron-bearing minerals are important to the adsorption of cesium (*4*, *7*).

Likewise, the mechanisms of uranium adsorption can vary depending on the mineral substrates to which the uranium is adsorbing. Several studies have shown that the adsorption of UO_2^{2+} onto montmorillonite is complex and due to several mechanisms: ion exchange (*8*−*10*), outer-sphere complex (*8*, *10*−*12*), or inner-sphere complex (*10*, *13*). Adsorption onto iron oxyhydroxides has been modeled with one type of adsorption site (*14*), an inner-sphere model (*15*), and high- and low-affinity sites (*16*, *17*). There is evidence for uranium incorporating into minerals when they transform from amorphous to crystalline structure (*18*, *19*). Adsorption of uranium in natural soils has been correlated to the iron content (*20*, *21*). Ferris et al. (*22*) presented a decrease in log K_d value with an increase in reducible iron oxide content of bacteriogenic iron oxides. It has been shown that iron hydroxides have a greater adsorptive capacity than clay minerals (*20*, *23*−*25*).

Thus, the delineation of clay versus iron oxyhydroxide content appears to be important in determining the extent and reversibility of adsorption of both cesium and uranium. This information, in turn, is important for the modeling of the transport of these metals at contaminated waste sites (e.g., Davis and Curtis (*26*)). For example, on the basis of the studies presented above, a soil with a higher clay content would be modeled differently (relative to kinetics and reversibility) for adsorption of cesium and uranium than a soil with iron oxyhydroxides as the major adsorbing phase. An understanding of the adsorption processes is necessary to know the appropriate distribution coefficient and which adsorption isotherm equation to use for an accurate transport model. An understanding of the mineral or iron content, in turn, will assist in determining which adsorption processes should be modeled.

We introduce computerized microtomography (CMT) as a simple, nondestructive, spatial high-resolution method to use on millimeter-scale materials to (1) map the iron content within the soil materials, (2) determine semiquantitatively the relative amounts of iron oxyhydroxides and iron-bearing clays, and (3) qualitatively image the adsorption of cesium (as a test case) and delineate the relationship of cesium adsorption with iron-bearing materials. A general background for X-ray CMT is provided by Flannery et al. (*27*). Other methods for characterizing the iron content of materials require chemical leaching or thin-sectioning samples and are often limited to imaging and analyzing only the accessible exterior surfaces (*1*). In contrast, the CMT method requires minimal sample preparation and allows for three-dimensional mapping at the micron scale that includes the simultaneous mapping of the interior and exterior of a

* Corresponding author phone: (505)844-2397; fax: (505)844-7354; e-mail: sjaltma@sandia.gov.
† Geohydrology Department, Sandia National Laboratories.
‡ University of Chicago.
§ Geochemistry Department, Sandia National Laboratories.

10.1021/es049103y CCC: $30.25 © 2005 American Chemical Society
Published on Web 03/15/2005

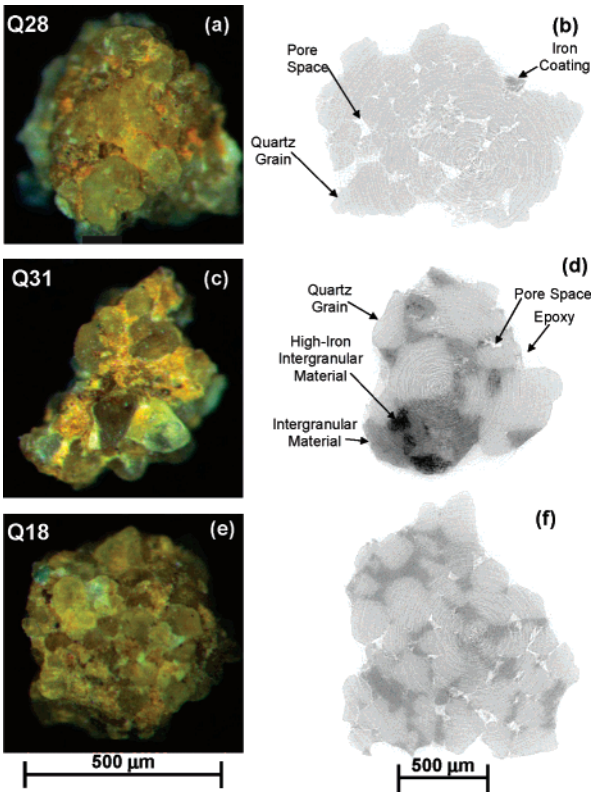

FIGURE 1. Optical photographs (a, c, e) and two-dimensional slices (b, d, and f) taken from three-dimensional tomographic images of aggregate samples, Q28 (a and b), Q31 (c and d), and Q18 (e and f). The darker the image, the higher the X-ray attenuation. Epoxy, quartz grains, and intergranular material are visible in the tomographic images of Q31 and Q18, whereas in the image of Q28 only a small area containing iron-bearing material can be seen. Note the areas of high X-ray absorbance within the intergranular material of Q31. Voxel size is 3.9 μm on a side. Three-dimensional images are available as Supporting Information.

sample. Because of the nondestructive nature of CMT, the method can be used to examine the complex relationships among coating mineralogy, mineral substrate, adsorption sites, and pore space. The methods presented here are meant to assist a researcher in characterizing the adsorptive properties of geological materials.

Experimental Section

Sample Description and Preparation. Soil samples were collected from a Uranium Mill Tailings Remedial Action (UMTRA) site in Naturita, Colorado (see Davis and Curtis (*26*) for a description of the hydrology and geochemistry of the site). An uncontaminated composite sample was collected from the alluvial plain of the San Miguel River several hundred yards upstream of the site of the former uranium processing mill. Cemented aggregate grains ranging from 0.14 to 0.19 cm were extracted by hand from the composite sample. Five samples were selected that appeared to be comprised of cemented quartz grains with some iron-based mineral coatings, on the basis of visual inspection under an optical microscope (Figure 1).

CMT images were collected on mineral samples of known composition for standardization purposes. The minerals used include iron-bearing clay samples of corrensite (CorWa-1) and ferruginous smectite (SWa-1) and low-iron clays Na-montmorillonite (SWy-2) and kaolinite (KGa-2) obtained from the Clay Minerals Society (*28*). These clays are all well-characterized and have accurately known mass fraction iron values. Research-grade siderite, hematite, and quartz obtained from Wards Natural Science were also imaged.

For the cesium-treated samples, the aggregate material was submerged in 507 g L^{-1} CsCl solution (400 g Cs L^{-1}) under a vacuum for at least 30 min. The pH of the solution prior to saturating the sample was 7.0. After removed from CsCl solution, samples were rinsed with deionized water. The rinse water was verified to be free of CsCl by testing for AgCl precipitation with a $AgNO_3$ solution. Cesium was chosen because of its high solubility and X-ray absorptive capacity. This high concentration of cesium was used to maximize the likelihood of detecting the adsorbed cesium with CMT. Altman et al. (*29*) demonstrated that in solution a concentration of 8 g of Cs L^{-1} or higher was needed to detect cesium, with higher concentrations leading to greater visualization capacity. The occurrence of CsCl precipitation on or in the samples is unlikely due to the solubility of CsCl being 1622 g L^{-1} in cold water (*30*).

All samples were mounted to a toothpick with epoxy. The toothpicks were inserted in the sample holder on the rotation stage for the CMT imaging and data collection.

Data Collection. Computerized microtomography data were collected at the Advanced Photon Source at Argonne National Laboratory. Data were obtained at Beamline 13-BM-D, operated by GeoSoilEnviroCARS (GSECARS) of the University of Chicago (*29*, *31*). Stampanoni et al. (*32*) provide a comprehensive description of a similar CMT system. The samples were rotated at 0.25° increments and imaged between 0° and 180°. The untreated samples (both aggregates and mineral standards) were imaged at 18 and 26 keV to maximize the X-ray attenuation due to the iron (optimal energy at or just above 7.112 keV) at the same time as optimizing the X-ray transmission through the sample. An energy level of 18 keV was determined to optimize X-ray transmission through our aggregate samples. However, this energy was too low to get sufficient transmission through the siderite mineral standard so duplicate measurements were made at 26 keV. The cesium-treated samples were imaged approximately 50−100 eV above and below the cesium absorption edge of 35.98 keV. The data were reconstructed using the methods of Dowd et al. (*33*). The data value for each voxel (three-dimensional data volume) is easily converted to the linear attenuation coefficient (μ) by knowing the voxel size. Linear attenuation coefficient [units = L^{-1}] is a measure of how absorptive the material is to X-rays (*34*).

Data Analysis. The average μ for each mineral standard was determined by defining a region of interest (ROI) that included only the mineral standard and then creating a distribution histogram of μ values within this ROI. The resulting histograms were best represented by a Gaussian distribution, defined by a mean and a standard deviation. Because of the well-defined Gaussian distributions, the signal noise about the mean was assumed to be random. The standard deviation was assumed to mostly be defined by the noise from the image collection process and to a lesser extent the heterogeneity within the sample. Average-measured μ was converted to average-measured mass attenuation coefficient (σ) [units = L^2 M^{-1}] using the known or estimated density (ρ) of the material:

$$\sigma = \frac{\mu}{\rho} \tag{1}$$

Regression relationships between average-measured σ and mass fraction iron were generated.

Histograms of the μ data collected from the aggregate samples were created. Gaussian distributions defining the surrounding air and epoxy, the quartz grains, and the intergranular material were delineated from these histograms. The mean μ for each region was determined from the Gaussian distributions. These mean μ values were confirmed

by identifying the different regions in the aggregate samples from visual inspection and calculating a mean μ for each separate region.

To calculate the mass fraction iron and mass fraction iron oxyhydroxide for the aggregate samples, we solved a system of four equations simultaneously using a Gauss−Seidel iterative method:

$$(f_{\text{Fe-Oxide}})(f_{\text{FeFe-Oxide}}) + (f_{\text{Clay}})(f_{\text{FeClay}}) = f_{\text{Fe}} \quad (2)$$

$$(f_{\text{Fe-Oxide}}) + (f_{\text{Clay}}) = 1 \quad (3)$$

$$\sigma = \frac{(f_{\text{Fe-Oxide}})\mu}{\rho_{\text{Fe-Oxide}}} + \frac{(f_{\text{Clay}})\mu}{\rho_{\text{Clay}}} \quad (4)$$

$$f_{\text{Fe}} = M + \sigma B \quad (5)$$

where $f_{\text{Fe-Oxide}}$, f_{Clay}, and f_{Fe} are the mass fraction iron oxyhydroxide, clay, and iron in the intergranular material, respectively; $f_{\text{FeFe-Oxide}}$ and f_{FeClay} are the mass fraction iron in the iron oxyhydroxide or clay, respectively; $\rho_{\text{Fe-Oxide}}$ and ρ_{Clay} are the densities of the iron oxyhydroxide and clay, respectively; M is the intercept and B is the slope of the regression line calculated using the mineral standards. It is assumed that the intergranular material is composed entirely of clay and iron oxyhydroxide. The linear attenuation coefficient, μ, is determined from our analysis of the experimental data, described above.

The system of equations was solved for all the combinations of the parameters to determine the probable maximum and minimum values of σ, $f_{\text{Fe-Oxide}}$, f_{Clay}, and f_{Fe}. Minimum and maximum values of some of our known parameters were used to determine the range for the unknown parameters. The minimum and maximum $f_{\text{FeFe-Oxide}}$ (0.58 and 0.63) assumed the iron oxyhydroxide was either goethite [$Fe^{+3}O(OH)$] or ferrihydrite [$Fe_5O_7OH{\cdot}4H_2O$]. The minimum and maximum f_{FeClay} (0.01 and 0.08) assumed the following stoichiometries for clay minerals in the Naturita samples on the basis of the work of Jové Colón et al. (*1*): $K_{0.31}Ca_{0.11}(Al_{1.41}Fe_{0.59})(Si_{3.42}Al_{0.53})O_{10}(OH)_2{\cdot}7H_2O$ and $K_{0.5}Ca_{0.2}(Al_{1.41}Fe_{0.11}Mg_{0.45})(Si_{3.42}Al_{0.53})O_{10}(OH)_2{\cdot}7H_2O$. The range in iron-oxyhydroxide densities was based on the densities of ferrihydrite (3.8 g cm^{-3}) and goethite (4.3 g cm^{-3}). Finally, we used a single value for the density of clay (2.6 g cm^{-3}) (*35*, *36*). This value was considered consistent with our assumed iron content of the clays (*1*).

Absorption edge difference images were generated on the Cs-treated samples. The difference images show where cesium is located within the sample (see Altman et al. (*29*) for more details on absorption edge difference imaging (AEDI)). We created the difference image by first ensuring that the two images were properly aligned and then subtracting the image taken below the absorption edge from that taken above the edge. A star-shaped object was epoxied onto the cesium-treated samples. The images of the star were used to make sure that this alignment was achieved.

We visually examined the images taken above and below the cesium X-ray absorption edge. Areas of high X-ray attenuation seen in the images taken below the absorption edge were assumed to be iron-bearing areas (at 35.88 keV, $\mu_{\text{Fe}} = 36.0\ \text{cm}^{-1}$, $\mu_{\text{CsCl solution}} = 2.7\ \text{cm}^{-1}$, $\sigma_{\text{Fe}} = 4.6\ \text{cm}^2\ \text{g}^{-1}$, $\sigma_{\text{CsCl solution}} = 1.8\ \text{cm}^2\ \text{g}^{-1}$). In contrast, in the images taken above the cesium absorption edge, high X-ray attenuation could be due to iron, cesium, or both (at 36.08 keV, $\mu_{\text{Fe}} = 35.4\ \text{cm}^{-1}$, $\mu_{\text{CsCl solution}} = 12.6\ \text{cm}^{-1}$, $\sigma_{\text{Fe}} = 4.5\ \text{cm}^2\ \text{g}^{-1}$, $\sigma_{\text{CsCl solution}} = 8.4\ \text{cm}^2\ \text{g}^{-1}$). The given μ and σ values for iron are for pure iron and thus overestimate the μ and σ for the iron-bearing materials. The difference image for each sample was qualitatively examined to see where the cesium was located and if there was a correlation between the cesium adsorption sites and the composition of the aggregate samples.

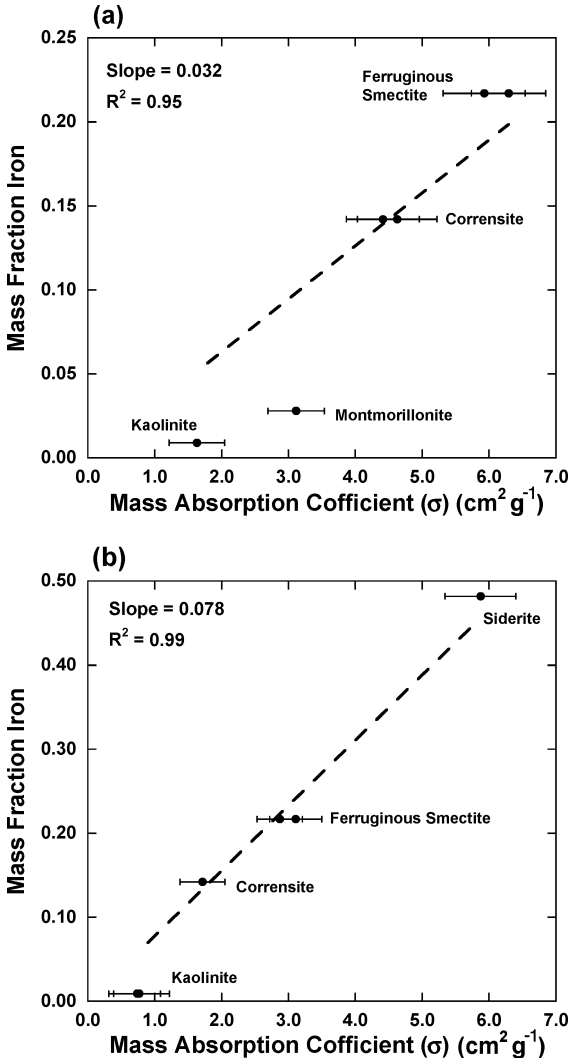

FIGURE 2. Regressions used to correlate measured σ with mass fraction iron for data collected at 18 keV (a) and 26 keV (b). Data were collected on mineral standards. Error bars represent ±1 standard deviation of the measured σ. The regression lines were forced to intercept the origin.

The results of this study are qualitatively compared to those of a parallel study using aggregate soil samples from the same field site (*1*). The latter study incorporated a combined suite of microbeam analytical techniques (scanning electron microscopy−energy dispersive spectrometry (SEM-EDS), secondary ion mass spectrometry, high-resolution transmission electron microscopy (HRTEM), microsynchrotron X-ray fluorescence (M-SXRF), and micro-X-ray absorption near-edge spectroscopy) to determine, in part, the composition of the fine-grained minerals coating the coarse mineral aggregates from Naturita. The authors identified mineral coatings comprised of interlayered illite−smectite clays and iron oxyhydroxide phases such as ferrihydrite and goethite.

Results and Discussion

Mineral Standard Analysis. An approximate linear relationship between σ and mass fraction iron in the mineral standards is observed (Figure 2). This observation supports our assumption that the iron content of the materials dominates X-ray attenuation. Kaolinite and montmorillonite do not fit the linear relationship as well as the other minerals.

The low-iron content of these minerals (less than 3%) most likely allows other components of the mineral to have a significant effect on X-ray attenuation. Siderite and hematite are not included in the regression generated with the 18 keV data and hematite is not included in the regression generated with the 26 keV data. This is because there was not enough X-ray transmission through the approximately 0.7-mm-diameter siderite sample and the 0.9-mm-diameter hematite sample to produce reliable data at the two different energies. The linear regression equations used to fit the data forced the regression line through the origin. Without this constraint, a negative intercept was obtained, which does not have a physical basis. Forcing the line through the origin (1) decreases the slopes slightly (0.050 to 0.032 for the 18 keV data and 0.090 to 0.078 for the 26 keV data), (2) decreases the calculated mass fractions for the 18 keV data, and (3) increases the calculated mass fractions for the 26 keV data. The changes in mass fraction iron were 1−4% for most of the intergranular material and 0−11% for the high-iron intergranular material.

Nanoscale porosity (porosity at a smaller scale than our voxel dimension) is not explicitly taken into account. Because an approximate linear relationship between σ and mass fraction iron was observed, we assume that nanoscale porosity is consistent between samples. Nanoscale porosity will lead to less X-ray absorbance than what is expected. Possible deviations from the linear trends could be explained by differences in this subvoxel scale porosity.

Aggregate Sample Analysis. The CMT images, with a voxel size of 3.9 μm on a side, qualitatively differentiate the quartz grains and iron-bearing intergranular or coating material (Figure 1). Pore space is visible within the samples (see Altman et al. (*29*) for further discussion). While samples Q28 and Q31 appear to have similar iron coatings from the optical photographs (Figure 1a and c), their interior composition is clearly different (Figure 1b and d). Iron-bearing interstitial material is not evident in the interior of sample Q28, although some iron coatings are observed. In contrast, sample Q18 appears to have a low-iron content from the optical photograph (Figure 1e), yet has significant iron-rich intergranular material (Figure 1f). On the basis of inspection of the CMT images, the grains in samples Q31 and Q18 appear to be much more rounded than those in Q28, where some euhedral material is visible. However, sample Q18 has much smaller grains than that of sample Q31, which could imply a different origin. Two distinct zones within the intergranular material of sample Q31 are noted, one of which is more absorbing to X-rays (higher iron content). The intergranular material in sample Q18 appears to be less absorbing to X-rays than that of sample Q31 (compare Figure 1f to Figure 1d). Images of the samples not shown (Q20 and Q25) are similar to that of Q31. Sample Q31 is the only sample where high-iron areas in the interstitial material strongly contrast the rest of the interstitial material in the CMT image.

The histograms of the μ values of each aggregate sample clearly delineate the quartz grains from the intergranular material (e.g., Figure 3). The mean value of the quartz grains for data collected at 18 keV is within 1−7% of what was measured from the pure quartz grain, reinforcing that these grains are truly quartz. For sample Q31 (Figure 3), a large tail can be seen in the region defining the intergranular material. This tail is assumed to be due to the intergranular material characterized by a high-iron content.

The estimates of iron content of the intergranular material are bound within 1−3%, depending on the sample and energy (Figure 4a). As explained in the data analysis section, these ranges are due to uncertainty in the iron oxyhydroxide density, mass fraction iron in the clay, and mass fraction iron in the iron oxyhydroxide. Iron content estimates are reproducible when multiple measurements were made on the same sample. The exception is the iron content estimate

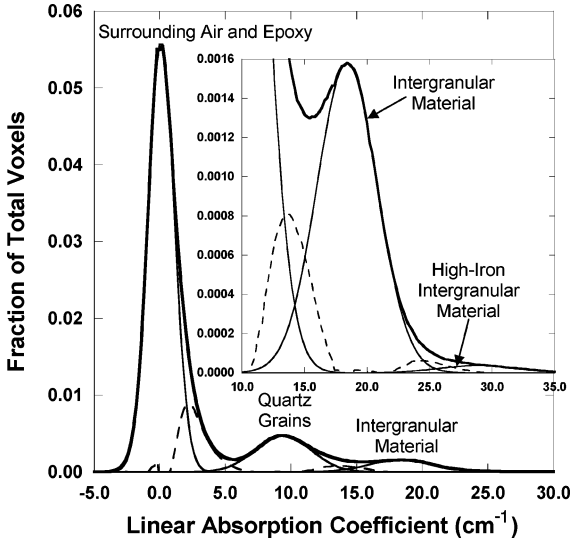

FIGURE 3. Histogram showing the fraction of voxels that are air or epoxy, quartz grains, and intergranular material for sample Q31. Inset is an enlargement of the intergranular portion of the histrogram showing the high-iron intergranular region. Heavy solid line is the histogram of the data. Light solid lines are the best-fit Gaussian distribution. Dashed lines delineate voxels that overlap two regions (mixed-value voxels).

for the high-iron intergranular material in sample Q31 where measurements made at 26 keV lead to a higher iron-content estimate.

Estimates of mass fraction iron oxyhydroxide are bound within 11% (Figure 4b). The fraction iron oxyhydroxide estimates are reproducible between different measurements made on the same sample, with the exception of the high-iron material in the intergranular material of sample Q31.

It is difficult to know whether the estimates of the mass fraction iron oxyhydroxide determined from the 18 keV data are more reliable than those estimated from the 26 keV data. At 18 keV ($\mu_{Fe} = 262.089$ cm^{-1}), the attenuation of X-rays due to iron is much stronger than at 26 keV ($\mu_{Fe} = 91.214$ cm^{-1}). Therefore, at this lower energy, there will be relatively less absorbance by the other elements in the mineral. However, at 18 keV the regression equation had to be extrapolated for σ values greater than approximately 6 cm^2 g^{-1}. This extrapolation could affect our estimates of σ for the high-iron intergranular material. This extrapolation was not necessary for the data collected at 26 keV.

With the possible exception of the areas of high-iron content in sample Q31, the intergranular material in all of the samples appears to be dominated by clay. There appears to be some variation in intergranular material composition between samples. Specifically, Q18 appears to have a lower mass fraction iron and slightly lower mass fraction iron oxyhydroxide than the other samples. This result is consistent with the qualitative differences noted in Figure 1. Perhaps the Q18 aggregate sample has a different origin.

Examination of the images of the cesium-treated samples indicated a correlation between the cesium-adsorption sites and the intergranular material in sample Q31 (Figure 5). For example, cesium can clearly be seen at approximately four and eleven o'clock positions in the difference image (Figure 5c), where intergranular material can be seen at these same locations in the image taken below the cesium absorption edge (Figure 5b). There also appears to be some cesium associated with the high-iron areas within the intergranular material at the six o'clock position. The intergranular areas at the edge of the aggregate where cesium is not observed are covered with epoxy. Unfortunately, the epoxy might have inhibited the migration of the cesium into these regions. In

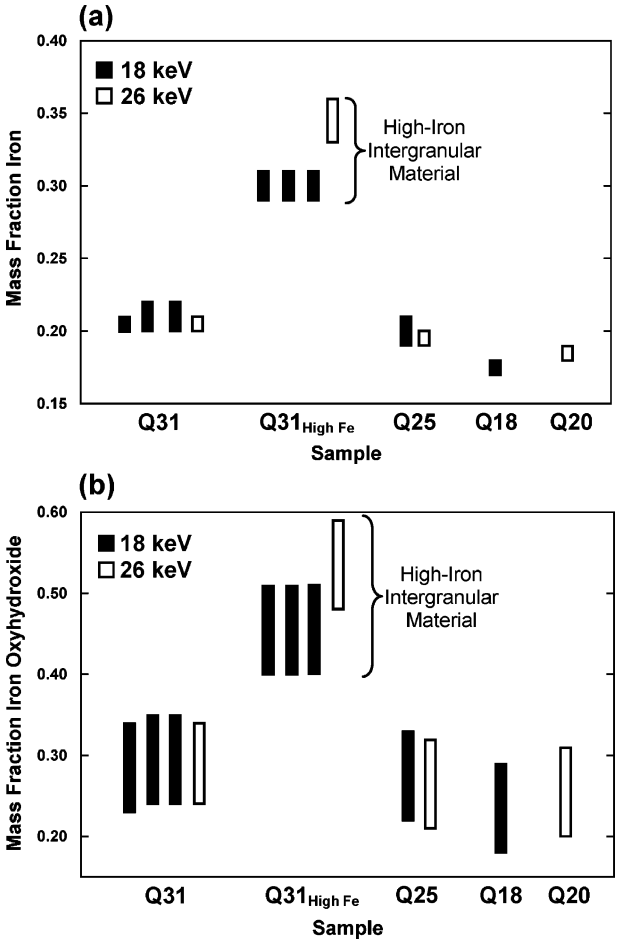

FIGURE 4. Approximated mass fraction iron (a) and mass fraction iron oxyhydroxide (b) in the intergranular material for different soil samples and multiple measurements of the same sample. Some measurements were made at 18 keV and others at 26 keV. Ranges in values represent uncertainty in the possible iron oxyhydroxide and clay composition. Mass fraction clay is assumed to be 1 minus mass fraction iron oxyhydroxide.

other areas (see Supporting Information), cesium is observed in the interior of the sample. Examination of other samples (not shown) also shows the correlation between the intergranular material and the cesium adsorption. Further studies on samples without epoxy blocking pore space is needed to confirm the correlation between the intergranular material and cesium adsorption.

Discussion. To further reduce the uncertainty in our results, we suggest collecting more data on standards that have a larger range of iron contents. These data would remove the need to extrapolate beyond the standards data to calculate σ for a sample. In addition, they could ensure a nonnegative intercept for the regression equation, unlike what we calculated. These data should also help resolve the differences we observed in our results for data collected at 18 and 26 keV.

Jové Colón et al.'s (*1*) work complemented this study by helping us estimate the formulation of the clays and the identity of iron oxyhydroxides. They demonstrated that illite/smectite clays and kaolinte coexist with iron oxides. Through HRTEM imaging, they show that both goethite and ferrihydrite also coexist. This information allowed us to determine the mass-fraction ratios of the clays to iron oxyhydroxides. However, this information is not needed to find the mass fraction iron using CMT. As long as one can bound the possible composition of an iron-bearing material being imaged, it would be possible to estimate the fractions of different minerals if their iron contents differ greatly from each other.

While Jové Colón et al. (*1*) were able to more definitively analyze the mineral content of the intergranular material, CMT has several advantages over their microanalytical methods. The spatial size of the images produced by HRTEM make it difficult to study an entire sample. CMT allows for mass fraction estimates of the different minerals within the high-iron intergranular material and estimates of the fraction of iron within the material. In contrast, the HRTEM images generated by Jové Colón et al. (*1*) only show that goethite is spatially much less abundant than the clay phases. In addition, CMT is a nondestructive method. With the intact sample, we were then able to examine the adsorptive capacity of the different regions in the sample. A transport experiment could be run through a column filled with the aggregated soil samples and CMT images collected periodically. Visualization of the location of the cesium in the aqueous and solid phase could assist in the interpretation of the cesium breakthrough curve.

The analytical methods described here could assist future studies in the evaluation of the adsorptive capacity of geological materials. Determining the iron content of a material or the mass fraction iron oxyhydroxide versus mass fraction iron of an iron-bearing clay could help a researcher develop a conceptual model of the adsorption process of different cations and, in turn, determine how they will numerically model the adsorption process in groundwater media. Taking the information of the iron oxyhydroxide versus iron-bearing clay content in conjunction with the available literature for different metal contaminants could help a researcher determine an appropriate distribution coefficient, or surface complexation model, and which adsorption isotherm equation to use to model their system.

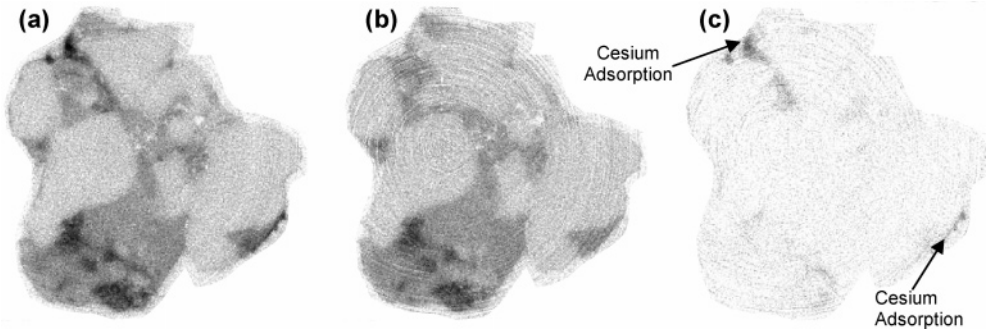

FIGURE 5. Images of cesium-treated sample Q31. Slices are taken from images collected above (a) and below (b) the cesium absorption edge and the difference image (c). Darker areas in a could be iron- or cesium-rich, darker areas in b are most likely iron-rich, and darker areas in c show where cesium is located. Slices extracted from the 3D image are approximately the same location as that shown in Figure 1. Voxel size is 3.9 μm on a side. Three-dimensional images are available as Supporting Information.

TABLE 1. Estimates of Mass Attenuation Coefficient (σ) ($cm^2\ g^{-1}$) for the Intergranular Material

sample ID	18 keV measurements	26 keV measurements
Q18	5.4−5.7	
Q20		2.3−2.5
Q25	6.1−6.5	2.4−2.5
Q31	6.2−6.5	2.6−2.7
	6.3−6.8	
	6.3−6.7	
Q31 (high iron)	9.0−9.7	4.2−4.6
	9.0−9.7	
	9.0−9.7	

However, modeling parameters are usually scale-dependent. Numerical or experimental upscaling exercises might be necessary to incorporate the information gained through CMT into larger-scale models. CMT therefore can assist in the development of a conceptual model and the numerical implementation and parametrization of fluid transport models. In addition, we have demonstrated how CMT in conjunction with AEDI can be used to visualize cesium on the intergranular material, presumably because of adsorption and possible exchange reactions. Evidence included the demonstration of the porous nature of the aggregate grains and the visualization cesium at the adsorption sites. The information that CMT provides can impact environmental evaluation and remediation of contaminated waste sites as well as the study of areas under consideration for nuclear waste disposal.

Acknowledgments

We would like to acknowledge the critical comments provided by four anonymous reviewers which greatly improved the final version of this manuscript. Carlos Jové Colón and Ray Finley are also thanked for their review. This project was funded by the U.S. Nuclear Regulatory Commission, Office of Nuclear Regulatory Research. We are grateful for the advice and support provided by our NRC program manager Edward O'Donnell. David Meese of the U.S.G.S. in Menlo Park is thanked for providing the soil sample. Sandia is a multiprogram laboratory operated by Sandia Corporation, a Lockheed Martin Company for the United States Department of Energy's National Nuclear Security Administration under Contract DE-AC04-94AL85000. GeoSoilEnviroCARS is supported by NSF-EAR-0217473, Department of Energy, Geosciences (DE-FG02-94ER14466), and the State of Illinois. Use of the APS was supported by the U.S. Department of Energy, Basic Energy Sciences, Office of Energy Research, under Contract W-31-109-Eng-38.

Supporting Information Available

Movies (MPEG files) of aggregate samples Q18, Q28, and Q31 imaged dry and sample Q31 after Cs treatment, imaged above and below the Cs-absorption edge and the difference image. This material is available free of charge via the Internet at http://pubs.acs.org.

Literature Cited

(1) Jové-Colón, C. F.; Sanpawanitchakit, C.; Xu, H.; Cygan, R. T.; Davis, J. A.; Meece, D. M.; Hervig, R. L. *A Combined Analytical Study to Characterize Uranium Soil Contamination*: *The Case of the Naturita UMTRA Site and the Role of Grain Coatings*; U. S. Nuclear Regulatory Commission: Washington, DC, 2005 (in review).

(2) Comans, R. N. J.; Haller, M.; De Preter, P. Sorption of cesium on illite: Non-equilibrium behaviour and reversibility. *Geochim. Cosmochim. Acta* **1991**, *55*, 433−440.

(3) Hsu, C. N.; Chang, K. P. Sorption and desorption behavior of cesium on soil components. *Appl. Radiat. Isot.* **1994**, *45*, 433−437.

(4) Cui, D.; Eriksen, T. E. On the sorption of Co and Cs on Stripa granite fracture-filling material. *Radiochim. Acta* **1997**, *79*, 29−35.

(5) Xiangke, W.; Wenming, D.; Zhi, L.; Jinzhou, D.; Zuyi, T. Sorption and desorption of radiocesium on red earth and its solid components: relative contribution and hysteresis. *Appl. Radiat. Isot.* **2000**, *52*, 813−819.

(6) Cornell, R. M. Adsorption of cesium on minerals: a review. *J. Radioanal. Nucl. Chem.* **1993**, *171*, 483−500.

(7) Gossuin, Y.; Colet, J. M.; Roch, A.; Muller, R. N.; Gillis, P. Cesium adsorption in hydrated iron oxide particles suspensions: an NMR study. *J. Magn. Reson. (USA)* **2002**, *157*, 132−136.

(8) Sylwester, E.; Hudson, E.; Allen, P. The structure of uranium (VI) sorption complexes on silica, alumina, and montmorillonite. *Geochim. Cosmochim. Acta* **2000**, *64*, 2431−2438.

(9) Hyun, S.; Cho, Y.; Hahn, P.; Kim, S. Sorption mechanism of U(VI) on a reference montmorillonite: binding to the internal and external surfaces. *J. Radioanal. Nucl. Chem.* **2001**, *250*, 55−62.

(10) Chisholm-Brause, C.; Berg, J.; Matzner, R.; Morris, D. Uranium-(VI) sorption complexes on montmorillonite as a function of solution chemistry. *J. Colloid Interface Sci.* **2001**, *233*, 38−49.

(11) Dent, A.; Ramsay, J.; Swanton, S. An EXAFS study of uranyl-ion in solution and sorbed onto silica and montmorillonite clay colloids. *J. Colloid Interface Sci.* **1992**, *150*, 45−60.

(12) Chisholm-Brause, C.; Conradson, S.; Buscher, C.; Eller, P.; Morris, D. Speciation of uranyl sorbed at multiple binding-sites on montmorillonite. *Geochim. Cosmochim. Acta* **1994**, *58*, 3625−3631.

(13) Hennig, C.; Reich, T.; Dahn, R.; Scheidegger, A. Structure of uranium sorption complexes at montmorillonite edge sites. *Radiochim. Acta* **2002**, *90*, 653−657.

(14) Morrison, S.; Spangler, R.; Tripathi, V. Adsorption of uranium-(VI) on amorphous ferric oxyhydroxide at high concentrations of dissolved carbon(IV) and sulfur(VI). *J. Contam. Hydrol.* **1995**, *17*, 333−346.

(15) Bargar, J.; Reitmeyer, R.; Lenhart, J.; Davis, J. Characterization of U(VI)-carbonato ternary complexes on hematite: EXAFS and electrophoretic mobility measurements. *Geochim. Cosmochim. Acta* **2000**, *64*, 2737−2749.

(16) Gabriel, U.; Gaudet, J.; Spadini, L.; Charlet, L. Reactive transport of uranyl in a goethite column: an experimental and modelling study. *Chem. Geol.* **1998**, *151*, 107−128.

(17) Waite, T.; Davis, J.; Payne, T.; Waychunas, G.; Xu, N. Uranium-(VI) adsorption to ferrihydrite: Application of a surface complexation model. *Geochim. Cosmochim. Acta* **1994**, *58*, 5465−5478.

(18) Payne, T.; Davis, J.; Waite, T. Uranium retention by weathered schists - the role of iron minerals. *Radiochim. Acta* **1994**, *66*−*7*, 297−303.

(19) Duff, M.; Coughlin, J.; Hunter, D. Uranium co-precipitation with iron oxide minerals. *Geochim. Cosmochim. Acta* **2002**, *66*, 3533−3547.

(20) Lumpkin, G.; Payne, T.; Fenton, B.; Waite, T. Preferential association of adsorbed uranium with mineral surfaces: a study using analytical electron microscopy. *Mater. Res. Soc. Symp. Proc.* **1999**, *556*, 1067−1074.

(21) Barnett, M.; Jardine, P.; Brooks, S.; Selim, H. Adsorption and transport of uranium(VI) in subsurface media. *Soil Sci. Soc. Am. J.* **2000**, *64*, 908−917.

(22) Ferris, F.; Hallberg, R.; Lyven, B.; Pedersen, K. Retention of strontium, cesium, lead and uranium by bacterial iron oxides from a subterranean environment. *Appl. Geochem.* **2000**, *15*, 1035−1042.

(23) McAlister, J.; Cooney, G.; Higgins, M. Accumulation of uranium in granitic soils overlying the Mourne Mountains, County Down, Northern Ireland. *Microchem. J.* **1997**, *56*, 315−326.

(24) Del Nero, M.; Salah, S.; Miura, T.; Clement, A.; Gauthier-Lafaye, F. Sorption/desorption processes of uranium in clayey samples of the Bangombe natural reactor zone, Gabon. *Radiochim. Acta* **1999**, *87*, 135−149.

(25) Casas, I.; Casabona, D.; Duro, L.; Depablo, J. The influence of hematite on the sorption of uranium(VI) onto granite filling fractures. *Chem. Geol.* **1994**, *113*, 319−326.

(26) Davis, J. A.; Curtis, G. P. *Application of Surface Complexation Modeling to Describe Uranium (VI) Adsorption and Retardation at the Uranium Mill Tailing Site at Naturita, Colorado*; Report NUREG/CR-6820; U. S. Nuclear Regulatory Commission: Washington, DC, 2003.

(27) Flannery, B. P.; Deckman, H. W.; Roberge, W. G.; D'Amico, K. L. Three-dimensional X-ray microtomography. *Science* **1987**, *237*, 1439−1444.

(28) Van Olphen, H.; Fripiat, J. J. *Data Handbook for Clay Materials and Other Non-Metallic Minerals*; Pergamon Press: New York, 1979.
(29) Altman, S. J.; Peplinski, W. J.; Rivers, M. L. Evaluation of synchrotron X-ray computerized microtomography for the visualization of transport processes in low-porosity materials. *J. Contam. Hydrol.*, in press (accepted November 30, 2004).
(30) *CRC Handbook of Chemistry and Physics*, 71st ed.; Lide, D. R., Ed.; CRC Press: Boca Raton, FL, 1990.
(31) Rivers, M. L.; Sutton, S. R.; Eng, P. Geoscience applications of X-ray computed microtomography. In *Proceedings of SPIE, Developments in X-ray Tomography II*; Bonse, U., Ed.; SPIE: Denver, 1999; Vol. 3772, pp 78−86.
(32) Stampanoni, M.; Borchert, G.; Wyss, P.; Abela, R.; Patterson, B.; Hunt, S.; Vermeulen, D.; Ruegsegger, P. High-resolution X-ray detector for synchrotron-based microtomography. *Nucl. Instrum. Methods Phys. Res., Sect. A* **2002**, *491*, 291−301.
(33) Dowd, B. A.; Campbell, G. H.; Marr, R. B.; Nagarkar, V.; Tipnis, S.; Axe, L.; Siddons, D. P. Developments in synchrotron. X-ray computed microtomography at the National Synchrotron Light Source In *Proceedings of SPIE, Developments in X-ray Tomography II*; Bonse, U., Ed.; SPIE: Denver, 1999; Vol. 3772, pp 224−236.
(34) Brown, J. G. *X-Rays and Their Application*; Plenum Press: New York, 1966.
(35) Mermut, A. R.; Cano, A. F. Baseline studies of the Clay Minerals Society source clays: Chemical analyses of major elements. *Clays Clay Miner.* **2001**, *49*, 381−386.
(36) Brindley, G. W.; Brown, G. *Crystal Structures of Clay Minerals and their X-ray Identification*; Mineralogical Society: London, 1980.

Received for review June 14, 2004. Revised manuscript received January 25, 2005. Accepted January 26, 2005.

ES049103Y